Transport and particle-hole asymmetry in graphene on boron nitride

Ashley M. DaSilva, Jeil Jung, Shaffique Adam, and Allan H. MacDonald

Transport and particle-hole asymmetry in graphene on boron nitride

Ashley M. DaSilva,[1] Jeil Jung,[2, 3] Shaffique Adam,[2, 4] and Allan H. MacDonald[1]

[1]*Department of Physics, The University of Texas at Austin, Austin, Texas 78712-1192, USA*
[2]*Graphene Research Centre and Department of Physics,*
National University of Singapore, 2 Science Drive 3, 117551, Singapore
[3]*Department of Physics, University of Seoul, Seoul, 130-743, Korea*
[4]*Yale-NUS College, 6 College Avenue East, 138614, Singapore*

All local electronic properties of graphene on a hexagonal boron nitride (hBN) substrate exhibit spatial moiré patterns related to lattice constant and orientation differences between shared triangular Bravais lattices. We apply a previously derived effective Hamiltonian for the π-bands of graphene on hBN to address the carrier-dependence of transport properties, concentrating on the conductivity features at four electrons and four holes per unit cell. These transport features measure the strength of Bragg scattering of π-electrons off the moiré pattern, and exhibit a striking particle-hole asymmetry that we trace to specific features of the effective Hamiltonian that we interpret physically.

I. INTRODUCTION

Boron nitride is a popular substrate for high quality graphene devices because it is atomically smooth, has low chemical reactivity, and is typically relatively free of defects.[1–5] These properties make it possible to achieve high graphene mobilities on hBN substrates. Hexagonal boron nitride (hBN) is a wide band gap semiconductor[6] with weakly coupled honeycomb lattice layers that are identical to graphene in structure, apart from a lattice constant difference of about two percent larger and possible differences in orientation. If the graphene and hBN lattices were perfectly matched, the graphene π electrons would inherent hBN's broken inversion symmetry and develop a finite energy gap at neutrality.[7,8] When exfoliated graphene is placed on a hBN surface, however, the two lattices do not align[2,9] and the electronic structure is more complex.[10,11]

In the most interesting case of nearly aligned layers, the two similar lattice periodicities lead to long-period moiré patterns[2,3,12] and to low-energy electronic properties that are insensitive to commensurability at an atomic level. Experiments show that in samples of this type a gap nevertheless appears at the Fermi level of a neutral sheet, and that its value is enhanced by electron-electron interactions and influenced by the strain patterns induced in the graphene sheet by the lattice constant mismatch.[13–15] At zero rotation angle (perfect alignment), the moiré wavelength is around 15 nm. In this case, secondary gapped Dirac points appear[9,11,12,16–18] at energies $\sim \pm$ 150 meV from the principal Dirac point, corresponding to the Fermi level of samples with ± 4 electrons per moiré period, corresponding to one full conduction band or one empty valance band, respectively. These electronic structure features are conveniently probed by studying the corresponding features in the carrier dependence of the dc transport properties of the graphene sheet. In this article, we present a theory of the transport properties of graphene on hexagonal boron nitride. We focus on the ± 4 electron-per-period features associated with the sec-ondary Dirac points, and in particular on the substantial particle-hole asymmetry which appears in all electronic properties, including the density of states.[12,17–19] We trace the asymmetry to the influence of the moiré pattern on inter-sublattice hopping terms in the graphene sheet Hamiltonian, and in particular to differences between the hopping amplitudes to nearest neighbor sites at carbon-above-boron and carbon-above-nitrogen positions.

Our paper is organized as follows. First in Section II we briefly summarize the moiré band Hamiltonian we use as the basis for our transport theory. In Section III we describe its band structure and discuss its density-of-states, carefully analyzing the origin of its particle/hole asymmetry. In Section IV we detail the transport theory we employ and in Section V we summarize its predictions for graphene on hBN. Finally, in Section VI we discuss and summarize our findings.

II. MOIRÉ BAND MODEL

The moiré band Hamiltonian we employ for the graphene sheet π-band electrons accounts for the influence of the substrate by adding a local sub-lattice dependent term to the $\mathbf{k} \cdot \mathbf{p}$ Dirac model of an isolated graphene sheet. The substrate interaction term has the same periodicity as the moiré pattern and, because it is periodic, can be analyzed using Bloch's theorem. The moiré band Hamiltonian yields a non-trivial band structure. It does not account for those features of the full Hamiltonian associated with atomic-scale commensurability and is accurate only for moiré pattern periods that greatly exceed the graphene sheet lattice constant. This however is the interesting case, because the influence of the substrate is weak for short moiré periods. The latter property can be traced[20] in part to the property that the distance between layers is substantially larger than the distance between atoms within a layer.

At a given position in the moiré pattern, the substrate interaction term in the moiré band Hamiltonian reflects

the local coordination between the graphene sheet and the substrate lattice, *i.e.* the positions of nearby boron and nitrogen atoms in the substrate relative to the positions of the carbon atoms in the graphene sheet. The substrate interaction term can be evaluated using *ab initio* methods[8,11] by calculating the rigid displacement dependence of the band Hamiltonian of commensurate honeycomb structures.

In this paper we use a moiré band Hamiltonian for graphene on hBN derived in this way. The moiré band Hamiltonian is able to account for the lattice mismatch of around 1.7 percent between graphene and hBN, and for strains in the graphene lattice and the substrate, and can be applied at any relative orientation between graphene sheet and substrate.[11] In a previous work we explained in detail how these effects combine with electron-electron interactions to control the size of the the gap which opens at the Fermi level of neutral graphene sheets, *i.e.* at the primary Dirac points in momentum space.[11] In this paper we will focus on the secondary Dirac points, and on gaps at the Fermi level of graphene sheets with ±4 electrons per moiré period. These features reflect the scattering of bare graphene sheet electrons off the periodic part of the substrate interaction Hamiltonian, whereas the neutral sheet gaps reflect mainly the spatial average of the substrate interaction Hamiltonian.

The moiré band Hamiltonian can be written as a sum of bare Dirac ($H_{\rm D}$) and substrate interaction ($H_{\rm M}$) contributions:

$$H = H_{\rm D} + H_{\rm M}. \qquad (1)$$

For practical calculations, we express this Hamiltonian operator as a matrix in momentum space:

$$\langle \mathbf{k}', s' | H | \mathbf{k}, s \rangle = \delta_{\mathbf{k},\mathbf{k}'} H_{\rm D}(\mathbf{k}) +$$
$$+ \sum_{\mathbf{G}} \langle s' | H_{\rm M,\mathbf{G}} | s \rangle \, \delta_{\mathbf{k}',\mathbf{k}+\mathbf{G}} \qquad (2)$$

where s and s' are sublattice indices, $\mathbf{k}$ and $\mathbf{k}'$ are wavevectors, $H_{\rm M,\mathbf{G}}$ is the Fourier transform of $H_{\rm M}(\mathbf{r})$ over one period of the moiré pattern, and $\mathbf{G}$ is a moiré pattern reciprocal lattice vector.

Ref. 11 discusses three versions of the moiré band Hamiltonian $H_{\rm M}$. In the first version neither graphene nor boron nitride atomic positions were allowed to relax under the the influences of inter-layer forces. This version gives very small band gaps at the primary Dirac point and is not consistent with experimental results. The other choices are to let just the graphene lattice relax, or to let both the graphene and boron nitride lattices relax. These lead to larger primary Dirac point gaps that are more in line with experimentally observed results, suggesting that strains play an essential role in samples with large period moiré patterns. In this paper we will use the version of the moiré band Hamiltonian that accounts for strains in both graphene and in the substrate, although we expect only relatively small quantitative substrate strain effects at the secondary Dirac points.
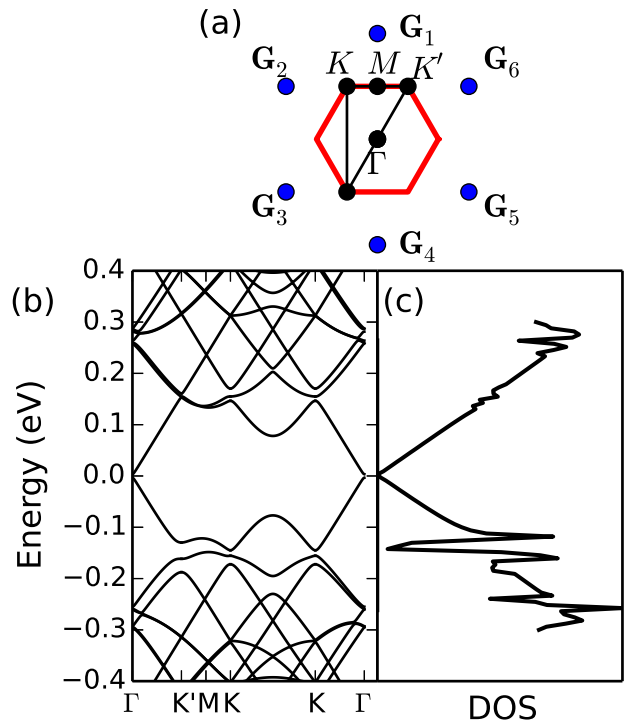

FIG. 1. Band structure and density of states of graphene on boron nitride. (a) Schematic illustration of the moiré pattern Brillouin zone, outlined in red. The blue dots are moiré pattern reciprocal lattice vectors. We label high symmetry points in the moiré Brillouin zone, Γ, M, and K at the Brillouin zone center, edge center, and corner points respectively, by black dots. (b) Moiré bands along the black lines in (a). (c) The density of states (horizontal axis) as a function of energy (vertical axis).

III. MOIRÉ BAND STRUCTURE AND DENSITY-OF-STATES

The moiré band structure and the density-of-states for the case of zero twist angle between graphene and substrate hexagonal lattices and a lattice constant mismatch of −0.017 are illustrated in Figure 1. Note that in addition to the small gap at the Dirac point, there are avoided crossings at the high-symmetry Brillouin-zone boundary points M and K. The electronic structure in this region of energy is highlighted in the Figure 2. Because distinct points on the Brillouin-zone boundary are connected by reciprocal lattice vectors, the size of the avoided crossing gaps is directly related to elastic scattering of bare graphene states off the substrate interaction Hamiltonian associated with the moiré pattern.

There is a distinct particle-hole asymmetry between the conduction and valence bands which is apparent in the density-of-states (Figure 1 (c)) and has been discussed previously in Refs. 12, 17, and 18, in terms of a phenomenological substrate interaction Hamiltonian in

(a) electrons

Energy (eV): 0.20 0.18 0.16 0.14 0.12 0.10

M

(b) electrons

Energy (eV): 0.20 0.18 0.16 0.14 0.12 0.10

K

(c) holes

Energy (eV): −0.10 −0.12 −0.14 −0.16 −0.18 −0.20

M

(d) holes

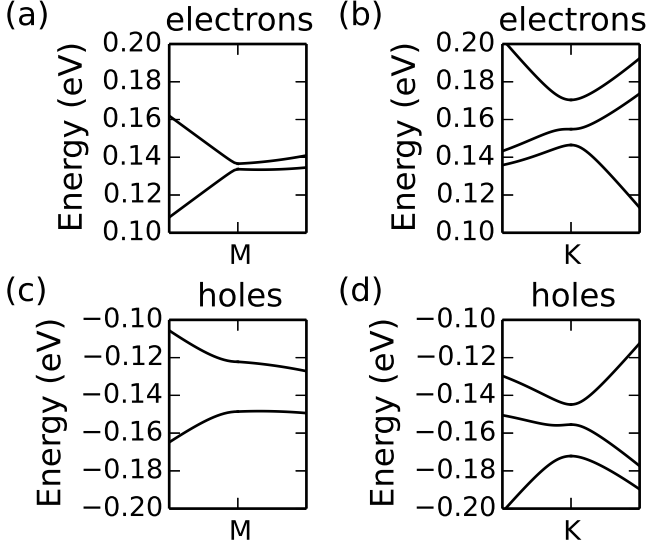Energy (eV): −0.10 −0.12 −0.14 −0.16 −0.18 −0.20

K

FIG. 2. Band structure near the secondary Dirac points. When substrate interactions are neglected, degeneracies forming secondary Dirac points occur at the M and K high-symmetry points defined in Figure 1. The substrate interaction Hamiltonian lifts these degeneracies. There are 2-band avoided crossing near the M point ((a) and (c)) and three band avoid crossings near the K point ((b) and (d)) in both the conduction band and the valence band.

which the number of free parameters has been minimized using symmetry considerations (the phenomenological substrate interaction Hamiltonian is compared with the interaction Hamiltonian derived from *ab initio* theory used here in Appendix A) and in Ref. 21 in terms of an effective Hamiltonian derived from a tight binding model.

To understand the physical mechanism behind this asymmetry, we use a nearly-free Dirac-electron approximation by treating the substrate-interaction Hamiltonian as a perturbation at the M point. When reduced to the Brillouin-zone, two eigenstates of the bare graphene Dirac Hamiltonian, corresponding to Dirac cones centered at $\mathbf{G}_0 \equiv 0$ and $\mathbf{G}_4 \equiv G(0, -1)$ are degenerate at the M point. Here $G \equiv |\mathbf{G}|$ is the magnitude of the primitive moiré reciprocal lattice vectors. The perturbed energies are,

$$E_{\pm}^{(b)} = E_{0,\mathrm{M}}^{(b)} \pm |U_b| \qquad (3)$$

where b is the band index (1 for conduction band and -1 for valence band), $E_{0,\mathrm{M}}^{(b)} = b\hbar v|G|/2$ is the energy of the bare Dirac Hamiltonian states at the M point,

$$U_b = \left(\psi_{\mathbf{G}_4}^{(b)}\right)^{\dagger} H_{\mathrm{M},\mathbf{G}_4} \psi_0^{(b)} \qquad (4)$$

and $\psi_{\mathbf{G}}^{(b)}$ is the wavevector-dependent sub lattice spinor of the unperturbed Dirac Hamiltonian. This leading order

perturbation theory analysis implies a band-dependent energy splitting at the M point equal to $\delta_{\mathrm{M},b} = 2|U_b|$.

To extract the physics behind the strong band dependence of this splitting, apparent in Figure 2 and indirectly in Figure 1, we decompose each Fourier component of the moiré band Hamiltonian into terms proportional to different sub lattice Pauli matrix contributions:[12,17,18,21,22]

$$H_{\mathrm{M},\mathbf{G}} = \sum_{\alpha=0,x,y,z} h_{\mathrm{M},\mathbf{G}}^{\alpha} \tau^{\alpha} \qquad (5)$$

(τ^0 is the 2x2 identity matrix). Note that the expansion into Pauli matrices is justified by the property that $H_{\mathrm{M}}(\mathbf{r})$ is Hermitian; the non-Hermitian character of $H_{\mathrm{M},\mathbf{G}}$ allows the expansion coefficients $h_{\mathrm{M},\mathbf{G}}^{\alpha}$ to be complex. For the $\hat{y}$-direction M-point, the bare sub lattice spinor has a pseudospin orientation proportional to the $\hat{y}$-direction momentum. It follows that,

$$\left(\psi_{\mathbf{G}_4}^{(b)}\right)^{\dagger} \tau^x \psi_0^{(b)} \approx bi \qquad (6)$$

$$\left(\psi_{\mathbf{G}_4}^{(b)}\right)^{\dagger} \tau^y \psi_0^{(b)} \approx 0 \qquad (7)$$

$$\left(\psi_{\mathbf{G}_4}^{(b)}\right)^{\dagger} \tau^z \psi_0^{(b)} \approx 1.0, \qquad (8)$$

and therefore that the coupling matrix element U_b is produced by the $h_{\mathrm{M},\mathbf{G}}^x$ inter sub lattice tunneling and the $h_{\mathrm{M},\mathbf{G}}^z$ sub lattice site-energy contributions to the substrate interaction Hamiltonian. The two sign choices in Eq. 6 correspond to conduction and valence bands. From the substrate interaction Hamiltonian

$$h_{\mathrm{M},\mathbf{G}_4}^x = (-0.70 - 7.31i)\ \mathrm{meV} \approx -7.3i\ \mathrm{meV} \qquad (9)$$

$$h_{\mathrm{M},\mathbf{G}_4}^z = (-5.63 - 0.36i)\ \mathrm{meV} \approx -5.6\ \mathrm{meV} \qquad (10)$$

it follows that the two contributions to U_b add in the valence band case and nearly cancel in the conduction band case. The final result is that the gap at the M point in the moiré Brillouin-zone is $\delta_{\mathrm{M},v} = 26$ meV in the valence band and almost an order of magnitude larger than in the conduction band where $\delta_{\mathrm{M},c} = 2.9$ meV.

Real space maps of the coefficients of the Pauli matrix expansion of the sub-lattice dependent substrate interaction Hamiltonian, $H_{\mathrm{M}}^x(\mathbf{r})$, $H_{\mathrm{M}}^y(\mathbf{r})$, and $H_{\mathrm{M}}^z(\mathbf{r})$, are provided in Figure 3. In our calculations the spatial origin is chosen to lie at an AA point in Figure 1. The relevant Fourier component for the matrix element we evaluate is G_4. The weighting factor in $h_{\mathrm{M},\mathbf{G}_4}^a$ is therefore complex conjugated when $y \to -y$ in Figure 3 where we see that H_{M}^z is approximately even and H_{M}^x is approximately odd. H_{M}^z provides a measure of the difference between site energies on the two graphene sub lattices. The difference between π-orbital energies is largest in magnitude when one carbon site is above the positively charged nitrogen site and the other is above the negatively charged boron site. At BA sites the carbon atoms above boron have a higher site energy than the the hexagonal plaquette centered carbon atoms, whereas at AB sites the plaquette

centered carbon atoms have a higher site energy than the carbon atoms above nitrogen. It follows that the on-site term H_M^z is negative at AA positions and positive at both AB and BA positions. The pseudospin term H_M^x provides a measure of differences between the hopping amplitudes from a carbon atom to its three near neighbors, and this difference vanishes by symmetry at AA, AB and BA sites. Carbon-carbon hopping is most anisotropic when one carbon atom is above the mid-point of a BN bond, and this leads to H_M^x values which have opposite sign at the mid-point between AA and AB points compared to the mid-point between AA and BA points, and therefore to $h_{M,\mathbf{G}_4}^x$ values that are approximately imaginary. We see therefore that the particle hole asymmetry is described correctly only when both site energy and hopping amplitude distortions are accounted for properly.

At the $\hat{y}$-direction K point, there are three approximately degenerate bands, corresponding to $\mathbf{G}_0 = 0$, $\mathbf{G}_4 = G(0, -1)$, and $\mathbf{G}_3 = G(-\sqrt{3}/2, -1/2)$. Perturbation theory (Appendix B) at K leads to a result that is similar to perturbation theory at M in that band separations are larger for the valence band than for the conduction band. Although the nearly-free-electron calculation is not as simple as in the two bands case, it is again true that a correct understanding of the origin of the strong particle-hole asymmetry requires an accurate account of substrate induced changes in both π-band energies and π-band hopping amplitudes.

IV. TRANSPORT THEORY

With this background established, we now explore the *dc* transport properties of graphene on boron nitride. One possible approach is to apply Boltzmann transport theory to the bands predicted by the moiré band Hamiltonian. This strategy is however reliable only when the associated Bloch state energy uncertainty, $\hbar/\tau$ where τ is the Bloch state lifetime, is small compared to the energy scale of band structure features. Because of the long period of the moiré pattern and the relatively weak strength of the substrate interaction, the largest band structure feature scale is the 26 meV valence band gap at four holes per moiré period explained in the previous section. We therefore choose an approach that is able to describe both weak and strong substrate interaction limits by applying a kinetic equation which is able to account for both intraband and interband contributions to the conductivity and using a relaxation time approximation for disorder. An overview of the theory is presented in this section, with details in Appendix C. The conductivity can be decomposed into intraband and interband terms, arising from scattering within a single band and scattering between bands. The intraband contribution is proportional to the density of states and the interband contributions become important when the spacings between bands close to the Fermi energy is smaller than $\sim \hbar/\tau$. In particular, because of the small band sepa-

rations at the Brillouin zone boundary, we anticipate a large interband contribution to the conductivity at four electrons per moiré period.

We obtain an estimate for the steady state density matrix by combining the equation of motion for the density-matrix (ρ) with a relaxation time approximation that accounts for the influence of disorder scattering on both band diagonal and band off-diagonal terms:

$$\frac{\partial \rho}{\partial t} = -\frac{i}{\hbar} [H, \rho] + \frac{1}{\hbar} \frac{\partial \rho}{\partial \mathbf{k}} \cdot e\mathbf{E} - \frac{\rho - \rho_0}{\tau} \qquad (11)$$

Here, H is the moiré band Hamiltonian in Equation (2), e is the magnitude of electric charge, $\mathbf{E}$ is the applied electric field, $\mathbf{k}$ is wave-vector in the moiré Brillouin zone measured from one of the graphene valleys, and τ is the relaxation time. The first term on the right-hand-side is purely off-diagonal in a moiré band Bloch representation and vanishes in equilibrium. The second term on the right-hand-side is the forcing term due to electric field, and the last term is the relaxation time approximation for scattering. We treat the relaxation time as an adjustable independent parameter, and assume that τ is the same for both intraband and interband scattering. In the steady state, $\partial \rho / \partial t = 0$. We expand this equation to linear order in the electric field $\mathbf{E}$, writing the density matrix, $\rho = \rho^{(0)} + \rho^{(1)}$, with $\rho^{(1)}$ being the linear response correction to the equilibrium moiré band density-matrix $\rho^{(0)}$:

$$\rho^{(0)} = \sum_{n\mathbf{k}} |n\mathbf{k}\rangle\langle n\mathbf{k}| \, f_{n\mathbf{k}} \qquad (12)$$

where n is a band index, and $f_{n\mathbf{k}}$ is one if the state is filled and zero if the state is empty. Since the first and third terms on the right-hand-side of Equation (11) are proportional to $\rho^{(1)}$, the kinetic equation is readily solved for the density-matrix linear response. The linear response current,

$$j_\alpha = \text{Tr} \{\rho^{(1)} \hat{j}_\alpha\} \equiv \sum_{n\mathbf{k}} \langle n\mathbf{k}|\rho^{(1)} \hat{j}_\alpha|n\mathbf{k}\rangle = \sum_{nm;\mathbf{k}} \rho_{nm}(-ev_D \tau^\alpha)_{mn}$$

$$= -ev_D \sum_{n\mathbf{k}} \left\{ \rho_{nn}^{(1)} \langle n\mathbf{k}|\tau^\alpha|n\mathbf{k}\rangle + \sum_{m \neq n} \rho_{nm}^{(1)} \langle m\mathbf{k}|\tau^\alpha|n\mathbf{k}\rangle \right\} \qquad (13)$$

$$\equiv j_{\alpha,intra} + j_{\alpha,inter} \qquad (14)$$

where $\alpha = x, y$ is the direction, $\hat{j}$ is the current operator and v_D is the Dirac velocity of graphene. Note that τ without a superscript refers to relaxation time, while τ^α with a superscript is a Pauli matrix. The conductivity can be correspondingly written as a sum of an intraband contribution due the dependence in Eq.(12) of band eigenenergies on $\mathbf{k}$ and interband contributions due
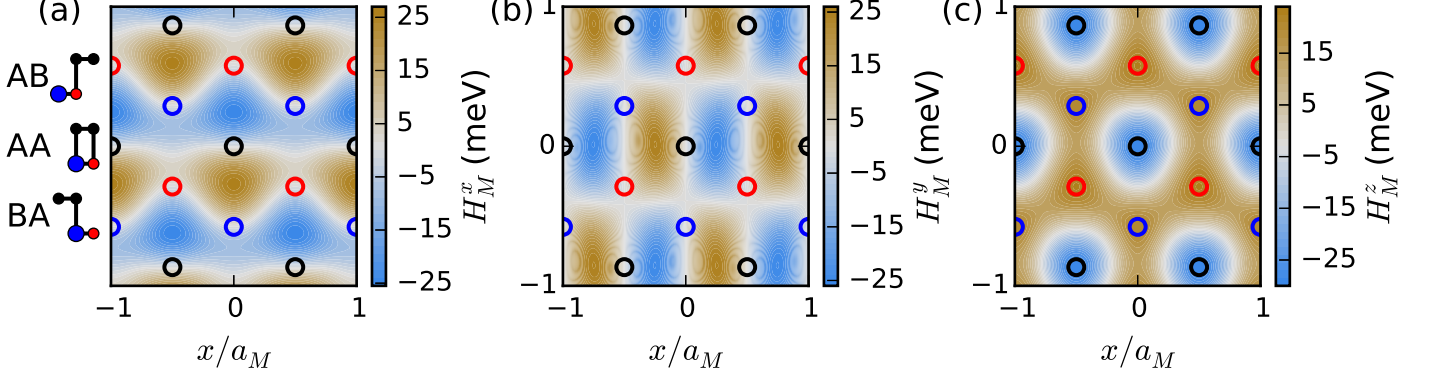
FIG. 3. Real space maps of the moiré-band Hamiltonian. The moiré Hamiltonian is local in position, but sublattice-dependent. At each position it can be decomposed into the sum of four terms proportional to Pauli matrices that act on sub lattice degrees of freedom. The x-component H_M^x is shown in (a), H_M^y in (b) and H_M^z in (c). For all subplots, the axes are in units of the moiré unit cell length, a_M. The open circles (color code explained by the cartoons in (a)) designate the positions within the moiré pattern of high-symmetry local stacking configurations. Red open circles correspond to AB (carbon above nitrogen) stacking, black to AA, and blue to BA (carbon above boron). In the cartoons, black dots are carbon atoms, reds are nitrogen, and blues are boron.)

to the dependence of $\mathbf{k}$ variation of band eigenstates:

$$\sigma_{\mathrm{intra}}^{\alpha\beta} = e^2 v_{\mathrm{D}}^2 \tau_1 \sum_{n\mathbf{k}} \delta(\varepsilon_{\mathrm{F}} - \varepsilon_{n\mathbf{k}}) \langle n\mathbf{k}|\tau^\alpha|n\mathbf{k}\rangle \langle n\mathbf{k}|\tau^\beta|n\mathbf{k}\rangle$$
(15)

$$\sigma_{\mathrm{inter}}^{\alpha\beta} = i e^2 \hbar v_{\mathrm{D}}^2 \sum_{n,\mathbf{k},m\neq n} \frac{f_{m\mathbf{k}} - f_{n\mathbf{k}}}{\varepsilon_{n\mathbf{k}} - \varepsilon_{m\mathbf{k}}} \frac{\langle n\mathbf{k}|\tau^\alpha|m\mathbf{k}\rangle \langle m\mathbf{k}|\tau^\beta|n\mathbf{k}\rangle}{\left(\varepsilon_{n\mathbf{k}} - \varepsilon_{m\mathbf{k}} + i\hbar\tau_2^{-1}\right)}$$
(16)

where $\varepsilon_{n,\mathbf{k}}$ is the energy of band n at wavevector $\mathbf{k}$ and $\tau_{1(2)}$ is the relaxation time for intra-(inter-)band scattering. The conductivity estimates summarized below were obtained by evaluating the sums in the above expressions numerically.

To capture qualitative experimental features realistically, we used mobility as a parameter and from this calculated a relaxation time proportional to mobility and energy, which is appropriate for a linear band structure.[23] The relaxation time for band b

$$\tau_b = \frac{\mu}{e} \frac{E}{v_b^2}$$
(17)

is dependent on the mobility μ, the energy E measured from the primary Dirac point, and an approximate band velocity v_b. In the absence of a moiré pattern this expression for the relaxation time is motivated by the experimental finding that the conductivity in graphene sheets is proportional to carrier density - i.e. that although the mobility can be sample dependent, it is approximately independent of density in individual samples. This property of graphene is related to the dependence of the disorder scattering amplitude on momentum transfer.[24–26] We calculate the band velocity by taking the average of

TABLE I. Table of band velocities and relaxation times for the six lowest energy bands of aligned graphene on boron nitride. The first two columns give the band edges, E_{min} and E_{max}. Band velocity, v_b is measured in units of the Dirac velocity for graphene, $v_D = 0.84 \times 10^6$ m/s. Both τ and $\hbar/\tau$ are given at an average band energy $E = (E_{\mathrm{max}} + E_{\mathrm{min}})/2$ for a sample mobility of $50,000$ cm^2/Vs. Note that according to our calculations there is a finite energy gap in the valence band which is indirect in moiré momentum space and therefore smaller than the local valence band gaps at individual momenta.

E_{min} (meV)	E_{max} (meV)	v_b/v_D	τ_b (ps)	$\hbar/\tau_b$ (meV)
-265	-170	0.393	9.9	0.066
-253	-147	0.752	2.5	0.26
-143	-1.71	0.916	0.61	1.1
5.31	155	0.969	0.60	1.1
138	260	0.801	2.2	0.30
163	266	0.447	7.6	0.087

the velocity along the direction from the moiré zone center to the zone corner (Γ to K in Fig. 1(a)), and the velocity along the direction from the zone center to the zone edge (Γ to M in Fig. 1(a)). We note that this procedure introduces a spurious reduction in the band velocity for the higher energy band of around 10 percent. While both this velocity averaging and the isotropic assumption for τ are rough estimates, we expect this approximation will capture the main features of the electron transport. Table I gives the average band velocities and representative relaxation times for the six lowest energy bands. For calculations of the mean free path and quantum transport for graphene on boron nitride without the effects of in-plane strain, we refer the reader to Ref. 19.
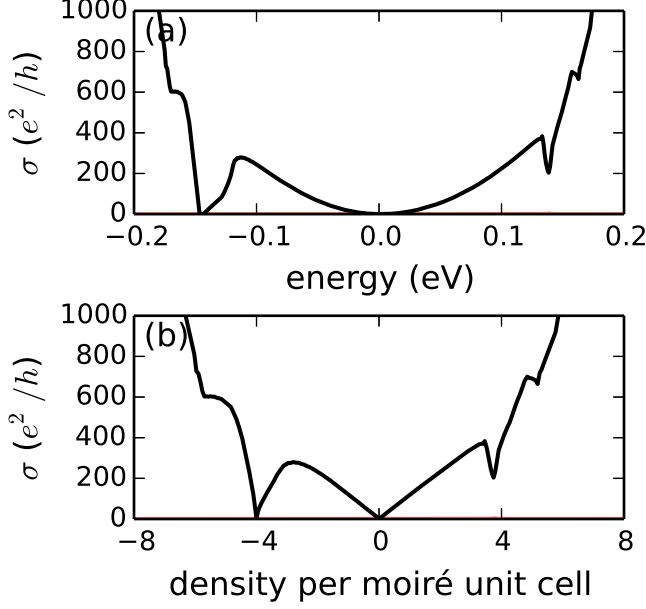
FIG. 4. The conductivity of graphene on hBN as a function of (a) energy and (b) density for a mobility of $50,000$ cm^2/Vs. In both plots the total conductivity is a solid black line. Features in the density of states (see Figure 1 (c)) have corresponding features in the intraband contribution to conductivity. The interband conductivity (red lines) is negligible at this mobility.

V. TRANSPORT THEORY RESULTS

The conductivity calculated for graphene on orientationally aligned hBN is plotted in Figure 4 both as a function of Fermi energy and as a function of carrier density. At high mobilities, the total conductivity is indistinguishable from the intraband contribution. Its features closely track the density of states. On the other hand, at low mobilities the interband contribution peaks when the Fermi level is close to weakly split Brillouin-zone edge states. Figures 5 and 6 show that while the interband contribution to the conductivity is generally quite weak, there is a peak on the conduction band side at a density close to four electrons per moiré period (red lines).

Figure 5 focuses on the strongest substrate related features in transport which appear when the Fermi level lies in the valence band at four holes per moiré period. Although much smaller, at $\delta_v \approx 3.5$ meV, than the splitting at individual k-points on the zone boundary, an overall gap does survive at this density. The gap is indirect in momentum space with the valence band maximum at the moiré M point and the conduction band minimum at the moiré K point, as seen in Figure 2 (c) and (d). When the mobility decreases $\hbar/\tau$ increases and the interband peak strengthens, slightly weakening the conductivity feature at 4 holes per moiré period; $\hbar/\tau$ is ~ 0.1 meV at this
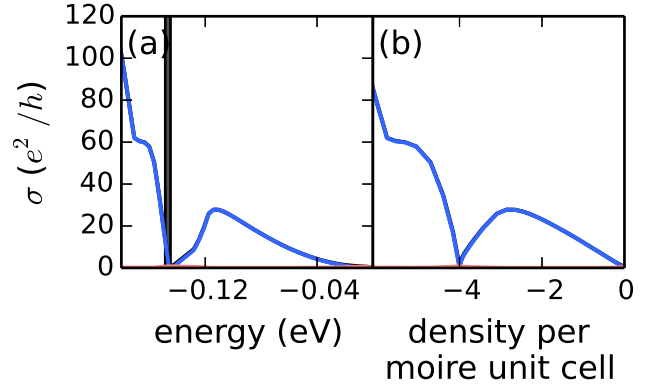

FIG. 5. Conductivity *vs.* hole density. (a) The conductivity as a function of Fermi energy for p-type systems. The intraband contribution is plotted in blue and the interband contribution in red. The gray shaded region indicates the energy range with the Fermi level in the gap at four holes per moiré period. (b) The conductivity as a function of hole density. The feature at four holes per moiré unit cell is due to the gap at this density. The calculations in this Figure are for a mobility of $5,000$ cm^2/Vs.
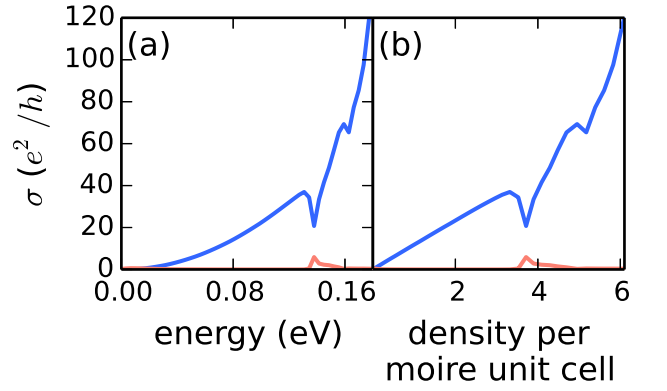

FIG. 6. Conductivity *vs.* electron density. (a) The conductivity as a function of Fermi energy for n-type systems. The intraband contribution is plotted in blue, the interband contribution in red. (b) The conductivity as a function of electron density. The feature at four electrons per moiré unit cell is due to the avoided band crossings at the Brillouin-zone boundary which are not sufficiently strong to yield an overall gap. The calculations in this Figure are for a mobility of $5,000$ cm^2/Vs. The interband contribution has peaks when the interband separation (see Figure 1 (b)) is smallest

energy in Figure 4 and $\hbar/\tau \sim 1.0$ meV at this energy in Figure 5. In both cases, $\hbar/\tau$ is much smaller than the band splitting, and therefore the interband scattering is negligible on the hole side.

A detailed look at the conduction band feature at a mobility of $5,000$ cm^2/Vs and four electrons per unit cell is provided in Figure 6. The intraband conductivity (blue lines) shows a dip when the Fermi level is close to the energies of the moiré Brillouin zone boundary avoided crossing states. There is no overall gap in the conduction
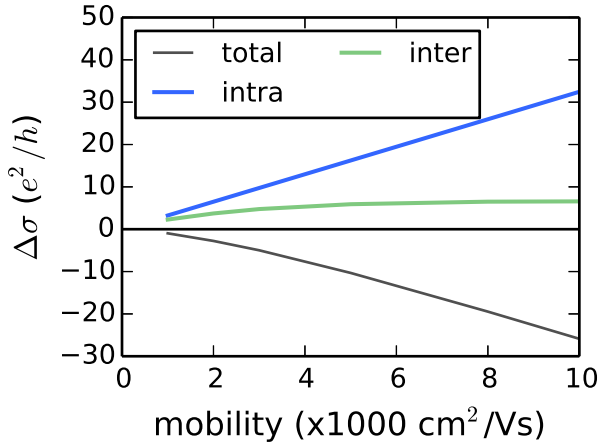
FIG. 7. Mobility-dependence of the conductivity feature at four electrons per moiré period. The size of the intraband conductivity (blue) dip and the interband conductivity peak (green) as a function of mobility. The total feature size is shown in black. For low mobility samples the relaxation approximation conductivity can have a peak rather than a dip at this density.

band, as shown in Figure 2, so there is a Fermi surface and an intraband contribution to transport at all energies in this interval, although the curve nevertheless has a dip. The peaks in the DOS are associated with saddle points in the moiré band structure. In particular, the first large peak is due to the saddle point at the M point in the first conduction band. The saddle point peaks are smoothed out in the conductivity calculation because of finite spectral widths associated with the finite Bloch state lifetimes. As shown in Figure 6 (b), the dip in intraband conductivity is partially compensated by a peak in the interband contribution shown in red in Figure 6. In Figure 7 we plot the magnitude of both features as a function of mobility. In the relaxation time approximation the intraband conductivity is proportional to mobility, and the intraband dip therefore dominates at high mobilities. In the same approximation, the peak in the interband contribution can strongly compensate at low mobilities.

Because the avoided crossing gaps on the moire band Brillouin-zone boundary are vastly larger in the hole carrier case than in the electron carrier case, the physics of the conductivity minimum is not the same. In the valence band case, the size of the gap is large compared to $\hbar/\tau$ and the interband contribution to the dc conductivity is negligible. In the conduction band case, the density of states does not vanish at any energy so the intraband conductivity is always finite. In addition avoided crossing gaps are not typically large compared to $\hbar/\tau$, allowing for a non-negligible interband contribution.

VI. SUMMARY AND DISCUSSION

We have calculated the band structure, the density of states, and the transport properties of graphene on hexagonal boron nitride at zero twist angle using a moiré band model. All exhibit a pronounced particle-hole asymmetry, which we have traced to a correlation between spatial variations of the difference between honeycomb sub lattice site energies, and spatial variations in intersublattice hopping amplitude properties. These variations are correlated because both are related to the charge difference between boron and nitrogen sites in the substrate. The difference between nearest neighbor hopping amplitudes in carbon-above-boron and carbon-above nitrogen regions plays a particularly essential role.

We focus our transport calculations on the first features in conduction and valence bands, where there are avoided crossings of the secondary Dirac points, corresponding to four carriers per moiré unit cell. The particle-hole asymmetry is seen in the transport. We find there is an overall gap of ~ 3.5 meV in the valence band, and no gap in the conduction band. We have included effects of interband and intraband response in the conductivity, the latter becoming important at lower mobility. In the relaxation time approximation, the interband dc conductivity has peaks at 0 and ± 4 electrons per moiré unit cell, which are not negligible for low mobility samples.

Experiments in graphene on boron nitride to date have focused on high-mobility samples, with mobilities as high as $275,000$ cm^2/Vs at low temperature.[27] Resistance peaks at 4 carriers per moiré unit cell and a distinct particle/hole asymmetry have been reported in Ref. 13 in high-mobility ($100,000$ cm^2/Vs) samples and in Ref. 28 for a sample of moderate mobility ($5,000$ cm^2/Vs) in agreement with our calculations. Although low mobility CVD graphene on SiO$_2$ and BN is available,[29] transport measurements of low mobility rotationally aligned samples have not been reported. The interband conductivity peak arises from large interband matrix elements of the current operator. We expect that optical experiments can readily probe this scattering mechanism in high mobility samples.[30]

tational resources from the Texas Advanced Computing Center.

Appendix A: Comparison between phenomenological and ab-initio substrate interaction Hamiltonians

Refs.17 and 18 formulate a symmetry-based phenomenological approach that can be used to construct effective Hamiltonians for graphene on substrates and leads to effective Hamiltonians of the form:

$$H = \hbar v \mathbf{k} \cdot \sigma + w_0 \hbar v G \sigma_0 + \tilde{w}_3 \hbar v G \sigma_3 \tau_3 + u_0 \hbar v G f_1(\mathbf{r}) + u_3 \hbar v G f_2(\mathbf{r}) \sigma_3 \tau_3 + u_1 \hbar v [\hat{z} \times \nabla f_2(\mathbf{r})] \cdot \sigma \tau_3 + u_2 \hbar v \nabla f_2(\mathbf{r}) \cdot \sigma \tau_3$$
$$+ \tilde{u}_0 \hbar v G f_2(\mathbf{r}) + \tilde{u}_3 \hbar v G f_1(\mathbf{r}) \sigma_3 \tau_3 + \tilde{u}_1 \hbar v [\hat{z} \times \nabla f_1(\mathbf{r})] \cdot \sigma \tau_3 + \tilde{u}_2 \hbar v \nabla f_1(\mathbf{r}) \cdot \sigma \tau_3$$
$$(A1)$$

where

$$f_1(\mathbf{r}) = \sum_{m=1}^{6} e^{i\mathbf{G}_m \cdot \mathbf{r}} \qquad (A2)$$

and

$$f_2(\mathbf{r}) = -i \sum_{m=1}^{6} (-1)^m e^{i\mathbf{G}_m \cdot \mathbf{r}} \qquad (A3)$$

The vectors $\mathbf{G}_m$ are the first shell of moiré reciprocal lattice vectors labeled as in Figure 1. We rewrite our effective Hamiltonian obtained by performing *ab initio* calculations in this phenomenological form.[31] In Table II we list the Hamiltonian parameters we obtain in this way for a lattice mismatch of $\varepsilon = -0.017$ and a zero twist angle. We note that including relaxation in the Hamiltonian significantly changes the values of the parameters. These differences in parameters are relevant for the interpretation of the particle-hole asymmetry in graphene on hBN.

TABLE II. Table of parameters for the Hamiltonian in Eqn. (A1) at $\varepsilon = -0.017$ and zero twist angle. The first column shows parameters for the Hamiltonian used in this paper. This Hamiltonian includes relaxation effects of the graphene and boron nitride lattices. The second column shows the parameters without including relaxation effects. Both these Hamiltonians are discussed in detail in Ref. 11. All quantities are in meV units.

	Relaxed	Rigid
$w_0 \hbar v G$ (meV)	0	0
$\tilde{w}_3 \hbar v G$ (meV)	3.74	0
$u_0 \hbar v G$ (meV)	1.26	−0.64
$\tilde{u}_0 \hbar v G$ (meV)	8.98	10.10
$u_1 \hbar v G$ (meV)	0.70	1.97
$\tilde{u}_1 \hbar v G$ (meV)	−7.31	−11.17
$u_2 \hbar v G$ (meV)	0	0
$\tilde{u}_2 \hbar v G$ (meV)	0	0
$u_3 \hbar v G$ (meV)	−0.36	1.26
$\tilde{u}_3 \hbar v G$ (meV)	−5.63	−8.89

Appendix B: Avoided crossing analysis at the moiré Brillouin zone corners

At each of the moiré Brillouin zone corners, there are three degenerate solutions to the gapped Dirac equation, $H_D + H_{M,\mathbf{G}=0}$ with a mass of $m = 3.7$ meV.[17,21] As in the case of the M point shown in the main text, we treat the off-diagonal terms in a degenerate perturbation theory. The energies are the eigenvalues of the 3×3 effective Hamiltonian,

$$H_{K,eff}^{(b)} = \begin{pmatrix} E_{0,K}^{(b)} & t_{3,b}^* & t_{4,b}^* \\ t_{3,b} & E_{0,K}^{(b)} & t_{5,b}^* \\ t_{4,b} & t_{5,b} & E_{0,K}^{(b)} \end{pmatrix} \qquad (B1)$$

where the index $\pm$ refers the conduction $(+)$ or valence $(-)$ band and

$$t_{j,b} = \left(\psi_{\mathbf{G}_i + \mathbf{G}_j}^{(b)} \right)^\dagger H_{M,\mathbf{G}_j} \psi_{\mathbf{G}_i}^{(b)} \qquad (B2)$$

The unperturbed energy on the diagonal is,

$$E_{0,K}^{(b)} = b\sqrt{m^2 + (\hbar v G/\sqrt{3})^2} \qquad (B3)$$

There are three eigenvalues of the Hamiltonian, labeled with subscript $i = 1, 2, 3$

$$E_i^{(b)} = E_{0,K}^{(b)} - w_i - \frac{|t_{3,b}|^2 + |t_{4,b}|^2 + |t_{5,b}|^2}{3w_i} \qquad (B4)$$

where w_i are the three solutions to the polynomial

$$w^6 + 2\text{Re}\,\{t_3^* t_5^* t_4\} w^3 + \left(\frac{|t_{3,b}|^2 + |t_{4,b}|^2 + |t_{5,b}|^2}{3} \right)^3 = 0 \qquad (B5)$$

which are guaranteed to be real since the Hamiltonian is Hermitian. Decomposing the moiré Hamiltonian into terms proportional to Pauli matrices,

$$H_{M,\mathbf{G}} = \sum_{\alpha=0,x,y,z} h_{M,\mathbf{G}}^\alpha \tau^\alpha \qquad (B6)$$

(τ^0 is the 2x2 identity matrix), we obtain values for $h_{M,\mathbf{G}}$ and $\left(\psi^{(b)}_{\mathbf{G}_i+\mathbf{G}_j}\right)^\dagger \tau^\alpha \psi^{(b)}_{\mathbf{G}_i}$ shown in table III. The situation is much more complicated than that of the M point, but the generic features remain: there is a sign change in the matrix elements of $\tau^{x,y}$ and not $\tau^{0,z}$, or vice versa, which results in constructive interference of different contributions to the $t_{i,b}$ values in the valence band and destructive interference in the conduction band. This leads to a smaller energy splittings in the conduction band.

Appendix C: Transport theory

The commutator, $[H, \rho]$, is

$$[H, \rho]_{nn'} = (\varepsilon_{nk} - \varepsilon_{n'k})\,\rho_{nn'} \tag{C1}$$

which vanishes when $n = n'$.

The derivative with respect to k of the equilibrium density matrix is,

$$\frac{\partial \rho^{(0)}}{\partial \mathbf{k}} = \sum_m \left\{ \frac{\partial f_{m\mathbf{k}}}{\partial \mathbf{k}} |mk\rangle\langle mk| + \right.$$
$$\left. + f_{m\mathbf{k}} \left| \frac{\partial}{\partial \mathbf{k}}\, mk \right\rangle \langle mk| + f_{m\mathbf{k}} |mk\rangle \left\langle \frac{\partial}{\partial \mathbf{k}}\, mk \right| \right\} \tag{C2}$$

The derivative of the wavefunction with respect to k is,

$$\left| \frac{\partial}{\partial \mathbf{k}}\, nk \right\rangle = \sum_{m\neq n} \left(\frac{\langle mk|\frac{\partial H}{\partial \mathbf{k}}|nk\rangle}{\varepsilon_{nk} - \varepsilon_{mk}} \right) |mk\rangle \tag{C3}$$

The only part of H which depends explicitly on $\mathbf{k}$ is $H_0 = \hbar v_{\mathrm{D}}\left(\tau^x, \tau^y\right)\cdot\mathbf{k}$ which has derivative with respect to k_α of $\hbar v_{\mathrm{D}}\tau^\alpha$. It follows that

$$\left(\frac{\partial \rho^{(0)}}{\partial k_\alpha} \right)_{nn'} = \delta_{nn'} \frac{\partial f}{\partial \varepsilon_{nk}} \langle nk|\hbar v_{\mathrm{D}}\tau^\alpha|nk\rangle +$$
$$+ (1 - \delta_{nn'})\langle nk|\hbar v_{\mathrm{D}}\tau^\alpha|n'k\rangle \frac{f_{n'\mathbf{k}} - f_{n\mathbf{k}}}{\varepsilon_{n'k} - \varepsilon_{nk}} \tag{C4}$$

Note that τ without a superscript refers to relaxation time, while τ^α with a superscript is a Pauli matrix. Using this in Equation (11) gives the expression for the current, Equation (13).

1 C. R. Dean, A. F. Young, I. Meric, C. Lee, L. Wang, S. Sorgenfrei, K. Watanabe, T. Taniguchi, P. Kim, K. L. Shepard, and J. Hone, Nature Nanotechnology **5**, 722 (2010).

2 J. Xue, J. Sanchez-Yamagishi, D. Bulmash, P. Jacquod, A. Deshpande, K. Watanabe, T. Taniguchi, P. Jarillo-Herrero, and B. J. LeRoy, Nature Materials **10**, 282 (2011).

3 R. Decker, Y. Wang, V. W. Brar, W. Regan, H.-Z. Tsai, Q. Wu, W. Gannett, A. Zettl, and M. F. Crommie, Nano Letters **11**, 2291 (2011).

4 S. Das Sarma and E. H. Hwang, Physical Review B **83**, 121405 (2011).

5 D. Wong, J. Velasco Jr., L. Ju, J. Lee, S. Kahn, H.-Z. Tsai, C. Germany, T. Taniguchi, K. Watanabe, A. Zettl, F. Wang, and M. F. Crommie, arXiv:1412.1878 [cond-mat] (2014), arXiv: 1412.1878.

6 K. Watanabe, T. Taniguchi, and H. Kanda, Nature Materials **3**, 404 (2004).

7 G. Giovannetti, P. A. Khomyakov, G. Brocks, P. J. Kelly, and J. van den Brink, Physical Review B **76**, 073103 (2007).

8 J. Jung, A. Raoux, Z. Qiao, and A. H. MacDonald, Physical Review B **89**, 205414 (2014).

9 C. Ortix, L. Yang, and J. van den Brink, Physical Review B **86**, 081405 (2012).

10 J. R. Wallbank, M. Mucha-Kruczynski, X. Chen, and V. I. Fal'ko, arXiv:1411.1235 [cond-mat] (2014), arXiv: 1411.1235.

11 J. Jung, A. M. DaSilva, A. H. MacDonald, and S. Adam, Nature Communications **6**, 6308 (2015).

12 M. Yankowitz, J. Xue, D. Cormode, J. D. Sanchez-Yamagishi, K. Watanabe, T. Taniguchi, P. Jarillo-Herrero, P. Jacquod, and B. J. LeRoy, Nature Physics **8**, 382 (2012).

13 B. Hunt, J. D. Sanchez-Yamagishi, A. F. Young, M. Yankowitz, B. J. LeRoy, K. Watanabe, T. Taniguchi, P. Moon, M. Koshino, P. Jarillo-Herrero, and R. C. Ashoori, Science **340**, 1427 (2013).

14 L. A. Ponomarenko, R. V. Gorbachev, G. L. Yu, D. C. Elias, R. Jalil, A. A. Patel, A. Mishchenko, A. S. Mayorov, C. R. Woods, J. R. Wallbank, M. Mucha-Kruczynski, B. A. Piot, M. Potemski, I. V. Grigorieva, K. S. Novoselov, F. Guinea, V. I. Falko, and A. K. Geim, Nature **497**, 594 (2013).

15 C. R. Woods, L. Britnell, A. Eckmann, R. S. Ma, J. C. Lu, H. M. Guo, X. Lin, G. L. Yu, Y. Cao, R. V. Gorbachev, A. V. Kretinin, J. Park, L. A. Ponomarenko, M. I. Katsnelson, Y. N. Gornostyrev, K. Watanabe, T. Taniguchi, C. Casiraghi, H.-J. Gao, A. K. Geim, and K. S. Novoselov, Nature Physics **10**, 451 (2014).

16 C.-H. Park, L. Yang, Y.-W. Son, M. L. Cohen, and S. G. Louie, Physical Review Letters **101**, 126804 (2008).

17 J. R. Wallbank, A. A. Patel, M. Mucha-Kruczynski, A. K. Geim, and V. I. Fal'ko, Physical Review B **87**, 245408 (2013).

18 M. Mucha-Kruczynski, J. R. Wallbank, and V. I. Fal'ko, Physical Review B **88**, 205418 (2013).

19 R. Martinez-Gordillo, S. Roche, F. Ortmann, and M. Pruneda, Physical Review B **89**, 161401 (2014).

TABLE III. Parameters for the analysis of the avoided crossing at the K point. The first three rows are the Pauli matrix decompositions of the moiré potential for values of reciprocal lattice vector relevant to the perturbation theory at the K point in the moiré Brillouin zone. The rest of the table shows the matrix elements of the Pauli matrices with the unperturbed wavefunctions at the given $\mathbf{G}$ values and $\mathbf{k}$ at the K point of the moiré Brillouin zone. Both conduction and valence band values are shown.

α	0	x	y	z
$h_{M,\mathbf{G}_3}^{\alpha}$ (meV)	$1.26 - 8.98i$	$0.350 - 3.66i$	$-0.606 + 6.33i$	$-5.63 + 0.36i$
$h_{M,\mathbf{G}_4}^{\alpha}$ (meV)	$1.26 + 8.98i$	$-0.699 - 7.31i$	0	$-5.63 - 0.36i$
$h_{M,\mathbf{G}_5}^{\alpha}$ (meV)	$1.26 - 8.98i$	$0.350 - 3.66i$	$0.606 - 6.33i$	$-5.63 + 0.364i$
Conduction band:				
$\left(\psi_{\mathbf{G}_3}^{(+)}\right)^{\dagger} \tau^{\alpha} \psi_{\mathbf{G}_0}^{(+)}$	$0.268 - 0.423i$	$-0.250 + 0.433i$	$0.433 - 0.750i$	$0.756 + 0.423i$
$\left(\psi_{\mathbf{G}_4}^{(+)}\right)^{\dagger} \tau^{\alpha} \psi_{\mathbf{G}_0}^{(+)}$	$0.268 + 0.423i$	$0.500 + 0.866i$	0	$0.756 - 0.423i$
$\left(\psi_{\mathbf{G}_4}^{(+)}\right)^{\dagger} \tau^{\alpha} \psi_{\mathbf{G}_3}^{(+)}$	$0.268 - 0.423i$	$-0.250 + 0.433i$	$-0.433 + 0.750i$	$0.756 + 0.423i$
Valence band:				
$\left(\psi_{\mathbf{G}_3}^{(-)}\right)^{\dagger} \tau^{\alpha} \psi_{\mathbf{G}_0}^{(-)}$	$-0.232 + 0.443i$	$-0.250 + 0.433i$	$0.433 - 0.750i$	$-0.744 - 0.443i$
$\left(\psi_{\mathbf{G}_4}^{(-)}\right)^{\dagger} \tau^{\alpha} \psi_{\mathbf{G}_0}^{(-)}$	$-0.232 - 0.443i$	$0.500 + 0.866i$	0	$-0.744 + 0.443i$
$\left(\psi_{\mathbf{G}_4}^{(-)}\right)^{\dagger} \tau^{\alpha} \psi_{\mathbf{G}_3}^{(-)}$	$0.232 - 0.443i$	$0.250 - 0.433i$	$0.433 - 0.750i$	$0.744 + 0.443i$

[20] R. Bistritzer and A. H. MacDonald, Physical Review B **84**, 035440 (2011).

[21] P. Moon and M. Koshino, Physical Review B **90**, 155406 (2014).

[22] M. Kindermann, B. Uchoa, and D. L. Miller, Physical Review B **86**, 115415 (2012).

[23] S. Das Sarma, S. Adam, E. H. Hwang, and E. Rossi, Reviews of Modern Physics **83**, 407 (2011).

[24] T. Ando, Journal of the Physical Society of Japan **75**, 074716 (2006).

[25] K. Nomura and A. H. MacDonald, Physical Review Letters **98**, 076602 (2007).

[26] S. Adam, E. H. Hwang, V. M. Galitski, and S. D. Sarma, Proceedings of the National Academy of Sciences **104**, 18392 (2007).

[27] P. J. Zomer, S. P. Dash, N. Tombros, and B. J. v. Wees, Applied Physics Letters **99**, 232104 (2011).

[28] W. Yang, G. Chen, Z. Shi, C.-C. Liu, L. Zhang, G. Xie, M. Cheng, D. Wang, R. Yang, D. Shi, K. Watanabe, T. Taniguchi, Y. Yao, Y. Zhang, and G. Zhang, Nature Materials **12**, 792 (2013).

[29] W. Gannett, W. Regan, K. Watanabe, T. Taniguchi, M. F. Crommie, and A. Zettl, Applied Physics Letters **98**, 242105 (2011).

[30] D. S. L. Abergel, J. R. Wallbank, X. Chen, M. Mucha-Kruczynski, and V. I. Fal'ko, New Journal of Physics **15**, 123009 (2013).

[31] Marcin Mucha Kruczynski, private communication.